Development of a new cryogenically cooled water vapor radiometer for the 22 GHz line - quasi-optical design and preliminary laboratory receiver tests

Adrianos Filinis[1,2], Alistair Bell[1,2], Axel Murk[1,2], and Gunter Stober[1,2]

[1]Institute of Applied Physics, University of Bern, Switzerland
[2]Oeschger Center for Climate Change Research, University of Bern, Switzerland

Correspondence: Adrianos Filinis (adrianos.filinis@unibe.ch)

Abstract. This paper reports on the instrumental design of a new cryogenically cooled middle-atmosphere water vapor radiometer developed by the University of Bern at the Institute of Applied Physics (IAP). Here, we present the instrument design for the breadboard stage. The key innovation of this new instrument is its cryogenically cooled front-end, which is designed to keep its size compact, reducing the required cooling power compared to existing cryogenically cooled radiometers. The advantage compared to uncooled instruments is the reduced receiver noise temperature and the possibility to extend the altitude coverage of the retrieval of water vapor profiles to even higher altitudes with better temporal resolution. The new radiometer is part of the Swiss H2O Hub and is supposed to replace the existing 22 GHz radiometer, MIAWARA, which has been in operation at the University of Bern for over 20 years at the Zimmerwald observatory. The calibration of the new instrument includes tipping curve calibration to determine tropospheric opacity, using the sky as a cold target. An ambient load serves as the hot target for the Hot-Cold calibration, and we also explore the possibility of using frequency-switch calibration to reduce the impact of non-linearities in the receiver chain, allowing for a higher integration time of the line observation compared to other calibration techniques. The combination of a cryogenic front-end and frequency switch microwave radiometers at 22 GHz has not been previously implemented in a single instrument. In addition to detailing the instrumental design and calibration techniques, we present preliminary results of atmospheric spectra obtained with the breadboard setup.

1 Introduction

Water vapor is an essential climate variable in the Earth's atmosphere and plays an important role in the radiative balance, serving as the most significant greenhouse gas in the upper troposphere (Andrews et al., 1987; Brasseur and Solomon, 2005). It plays, together with ozone and carbon dioxide, a pivotal role in the radiative cooling of the stratosphere and mesosphere through infrared emissions (Andrews et al., 1987). It participates in various chemical reactions and influences polar ozone chemistry through heterogeneous processes on the surfaces of polar stratospheric clouds (PSC). During cold conditions, ice

PSC formation followed by sedimentation can remove H_2O from the gas phase ("freeze drying"), and since stratospheric OH is produced mainly via $O(^1D) + H_2O \longrightarrow 2\,OH$ (with $O(^1D)$ originating from ozone photolysis), this dehydration directly affects the local HO_x radical budget (Steiner et al., 2021). In the stratosphere and mesosphere, water vapor has a longer chemical lifetime compared to the timescales of dynamic processes, making it a useful tracer for studying phenomena like the vertical transport due to the residual circulation at mesospheric altitudes (Straub et al., 2012; Shi et al., 2023), meridional transport, and the containment of the polar vortex as well as more rapid vertical coupling processes such as Sudden Stratospheric Warmings (SSWs) (Seele and Hartogh, 2000; Schranz et al., 2020; Shi et al., 2024, 2025).

Water vapor in the upper stratosphere and mesosphere is primarily monitored through passive remote sensing, either from space-based or ground-based instruments. Satellites like MLS on EOS/Aura (Waters et al., 2006), MIPAS on ENVISAT (Milz et al., 2005), and ODIN (Murtagh et al., 2002) provide both vertical and global data coverage, while ground-based instruments offer vertical profiles at specific locations. Ground-based instruments are characterized by long operational lifetimes, while the lifetime for satellites is typically limited to less than 10 years, although SABER on board TIMED and MLS on AURA achieved mission lifetimes of 2 decades and beyond. Ground-based measurements are essential for the long-term monitoring of water vapor and to ensure a reliable and resilient reference baseline that is a precious source to combine consecutive satellite missions, allowing the creation of continuous global datasets that are vital for climate research. For profiling middle atmospheric water vapor from the ground, the rotational transition at 22 GHz is typically utilized due to the low tropospheric opacity at this frequency, making it observable even from sea level.

Only a few ground-based spectro-radiometers operate regularly at 22 GHz, such as the instruments in Kiruna (Sweden) (Seele and Hartogh, 1999) (which operated in Norway in Andenes as well), and Seoul (South Korea) (De Wachter et al., 2011), as well as those in the NDACC (Network for the Detection of Atmospheric Composition Change) network at sites like Onsala (Sweden) (Forkman et al., 2003), Bern (Switzerland) (Deuber et al., 2004a; Bell et al., 2025), Table Mountain (California, USA), Mauna Loa (Hawaii, USA), and Lauder (New Zealand) (Thacker et al., 1995; Nedoluha et al., 1997, 2007). Additionally, several new instruments have been developed in recent years, including those at Zugspitze (Germany) (Hallgren et al., 2013), Karlsruhe (Germany), and the Mobile Microwave Radiometer operated by the University of Toulouse (France) (Motte et al., 2008).

The demand for water vapor measurements has increased rapidly in recent years due to the Hunga Tonga–Hunga Ha'apai's volcanic eruption on 15th January 2022 (Wright et al., 2022; Carr et al., 2022; Matoza et al., 2022), which injected a big anomaly of water vapor, that was first detected from MLS by Khaykin et al. (2022), and detected the H2O zonal mean anomalies in the tropics by Millan et al. (2022). In addition, with the planned stop of the Aura MLS 190-GHz observations (specifically of H2O, N2O, HCN, and upper stratospheric HNO3), there is a need for newly developed radiometers. As part of the Swiss H2O Hub(Federal Office of Meteorology and Climatology MeteoSwiss), the design of a new cryogenically cooled 22 GHz radiometer for stratospheric and mesospheric water vapor profile measurements was launched.

Here we present the design and first breadboard of our third-generation 22 GHz microwave radiometer for middle atmospheric water vapor retrievals. The first instrument, the Middle Atmospheric WAter vapor RAdiometer (MIAWARA) (Deuber et al., 2004a), began routine operation near Bern in 2002 and has been part of NDACC since 2005. The Stratospheric WAter Vapor RAdiometer (SWARA) (De Wachter et al., 2011), is a collaborative project between the University of Bern and Sookmyung

Women's University in Seoul, South Korea, and began operation in Seoul in 2006 as a replica of MIAWARA. The third, the Middle Atmospheric WAter vapor RAdiometer for Campaign (MIAWARA-C) Straub et al. (2010), began operation in 2008 in Bern, Switzerland, and is currently stationed in Ny-Ålesund since 2015.

The new instrument will have a cryogenically cooled front-end and leverage the receiver design from other instruments. The advantage of cooling the first stage of the front-end is to reduce the receiver noise temperature and, thus, to improve the signal-to-noise ratio. This is a prerequisite to enhance the sensitivity of the instrument, which results in an improved altitude coverage up to altitudes of 85 km as well as a better temporal resolution compared to the uncooled MIAWARA and MIAWARA-C.

A key goal of our design is that the calibration scheme of CRYOWARA is independent of any other instruments and requires no liquid nitrogen. Instead, the cold sky is used as a cold target for tipping curve calibration. In parallel, a permanently installed ambient target is used to routinely perform the hot-cold calibration. Furthermore, we are experimenting with a novel approach for the 22 GHz line by applying a frequency switching to reduce and mitigate the impact of any non-linearities in the system.

The manuscript is structured as follows. In section 2 of this paper, we present the instrumental setup, focusing on the optical design and the front-end embedded into a vacuum chamber. The 3rd section focuses on a comparison with MIAWARA, investigating the benefits of the new radiometer. The 4th section presents the calibration scheme. In section 5, we present some early results from the breadboard design and, lastly, the future steps of the radiometer.

2 CRYOWARA instrumental design

Similar to previous instruments, such as MIAWARA and MIAWARA-C, CRYOWARA is designed to observe the 22 GHz pressure-broadened water vapor line with a sufficient bandwidth to perform retrievals covering the altitude range from 30-85 km. The main challenge in the design of CRYOWARA was to reduce the feedhorn and front-end physical dimensions to achieve the desired size of the vacuum chamber. The more compact these parts of the instrument are designed, the easier it is to control the temperature of the feedhorn and the front-end. Therefore, the quasi-optic design was guided by minimizing the physical dimensions of each component without sacrificing the performance goals.

2.1 Optical setup

A broad overview of the instrumental design is given in Figure 1 and Figure 2. The instrument was designed to achieve the performance specifications summarized in Table 1. The instrument is divided into 3 parts: 1) the mirror, 2) the cryogenic front-end, and 3) and digital back-end. A parabolic mirror is chosen to direct the atmospheric microwave signal in the vacuum chamber through a microwave window to the cooled corrugated feedhorn antenna. The feedhorn antenna is designed for dual-polarization observation, which results in an increased signal-to-noise ratio. However, our receiver is not correlating both polarizations, considering that the water vapor line is an unpolarized emission, whereas, for example, the TEMPERA-C radiometer is fully polarimetric (Krochin et al., 2022, 2025). Nevertheless, the signal is divided into horizontal and vertical polarization by an ortho-mode transducer before being amplified by the two cryogenically cooled amplifiers. They are cooled by 2 copper braids attached to the cryocooler. The signal of each polarization passes through a high-pass filter with a cutoff

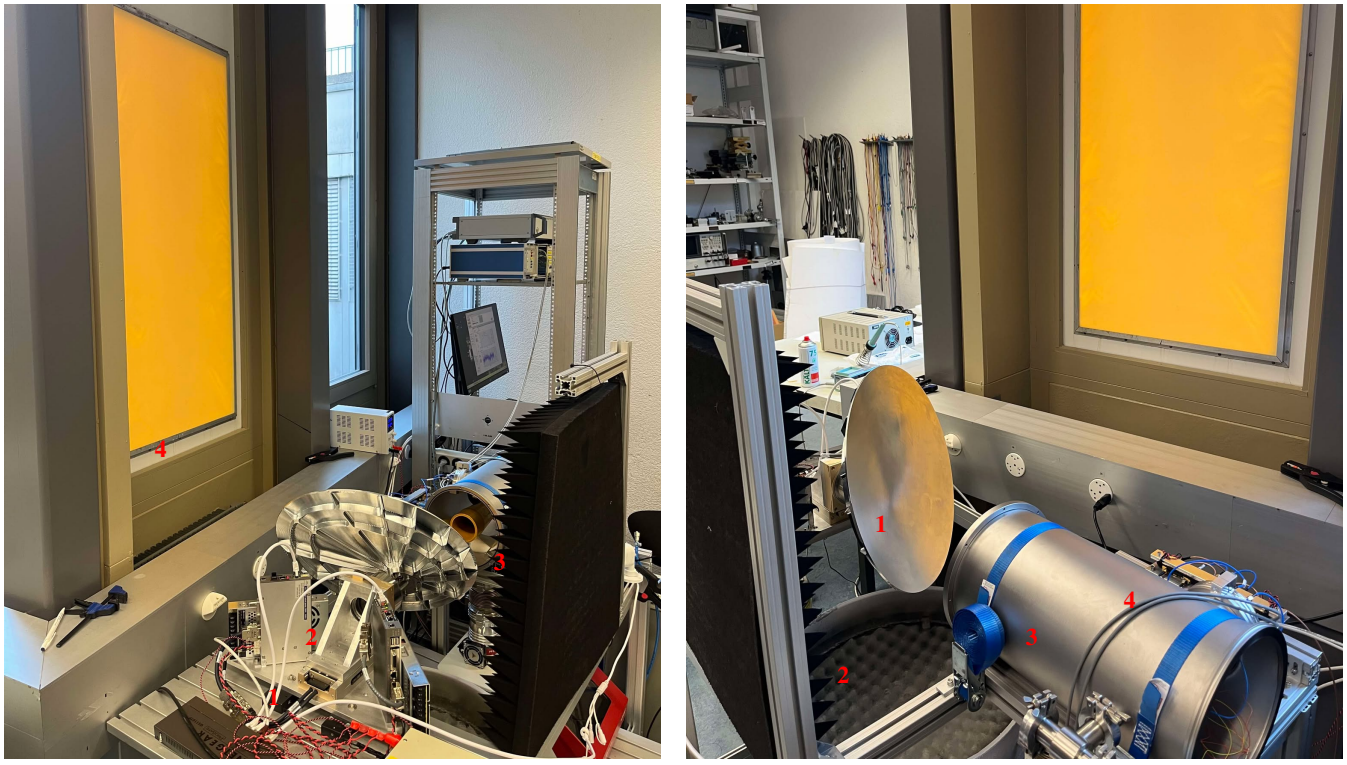

Figure 1. Breadboard assembly of CRYOWARA during first calibration observing the sky at 45° elevation angle. Left panel: 1) Linear stage, 2) Rotating stage, 3) Ambient target, 4) Transparent microwave window, and right panel: 1) Parabolic reflector, 2) LN2 target, 3) Vacuum chamber, 4) front-end chain.

frequency at 21 GHz, which ensures single sideband operation of the following heterodyne mixer. The mixer is pumped with an LO signal around 18 GHz to down-convert to the intermediate frequency of 4 GHz. The intermediate frequency signal is further amplified before entering the spectrometer.

The spectrometer is part of the back end. The breadboard setup operates with a USRP X310 with two UBX daughter boards,

Table 1. Design specifications for the new radiometer.

Design specifications
full-width-half-maximum (FWHM): 3 degrees
Corrugated horn sidelobes < -30 dB
Parabolic reflector spillover < -30 dB
Dual polarization receiver chain
Cryogenic cooled front end

which provide two input channels with 200 MHz bandwidth. The digitized data of each polarization is processed by a real-

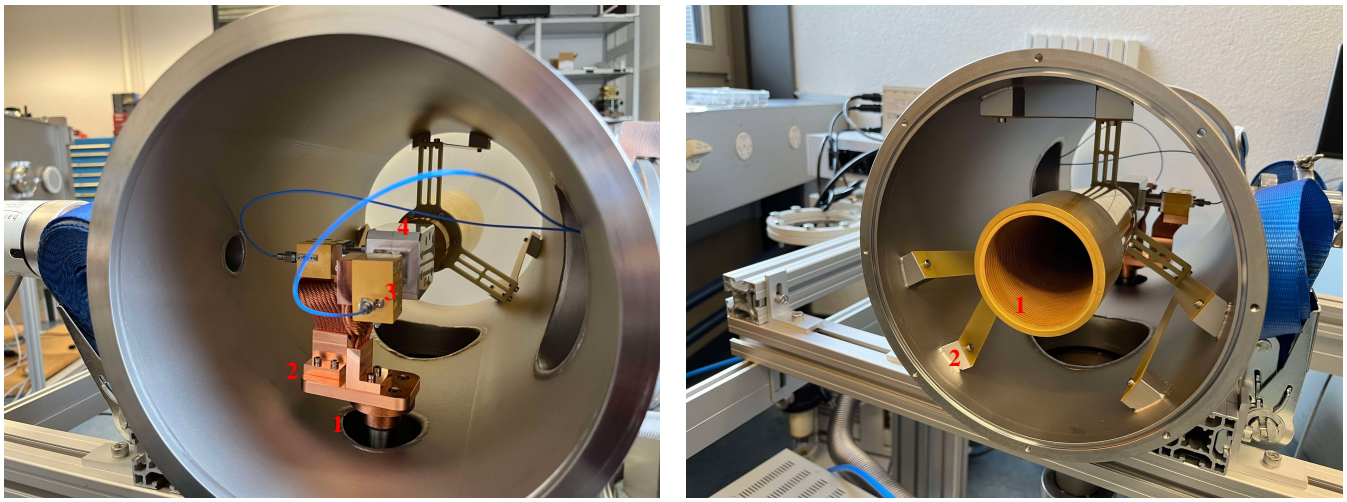

Figure 2. Breadboard assembly of CRYOWARA, assembly of vacuum chamber. Left panel: 1) Cryocooler cold head, 2) Copper bread, 3) Low noise amplifier (LNA) and coaxial cable, 4) Ortho mode transducer (OMT), and right panel: Gold-plated corrugated profiled antenna designed for 22 GHz, 2) Corrugated antenna mounting structure, material G10.

time Fast Fourier Transformation (FFT) with 16384 channels, resulting in a frequency resolution of 12.2 kHz. The bandwidth and frequency resolution of CRYOWARA are sufficient to retrieve water vapor profiles from 30 to 85 km altitude based on simulations with the Atmospheric Radiative Transfer Software (ARTS).

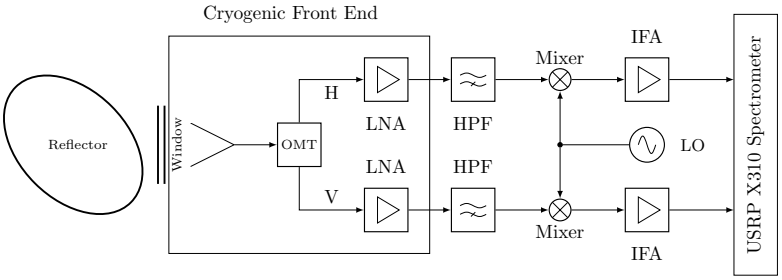

Figure 3. Schematic diagram of the CRYOWARA radiometer with the reflector, window, feed horn, ortho-mode transducer (OMT), cryogenically cooled low noise amplifiers (LNA), high-pass filters (HPF), mixers, local oscillator (LO), intermediate frequency amplifiers (IFA), and the spectrometer.

2.1.1 Quasi Optical design

For the quasi-optical design, the corrugated feedhorn antenna, with and without the microwave window, and the parabolic reflector have been designed with the antenna simulation software packages GRASP and CHAMP from the company TICRA (TICRA, 2024). The software has the option to take the exterior of the corrugated feed into account, to include the vacuum

window in the simulations, and to simulate the spillover and the far-field of the parabolic reflector. For middle atmospheric water vapor soundings, a narrow antenna beam is beneficial; narrow refers here to a beamwidth of FWHM 3°, Deuber et al. (2004b) simulated the difference in brightness temperatures for different elevation angles for different beamwidths and showed a nonlinear increase with beamwidth and found that a FWHM of 3° is often an acceptable compromise. Considering that the difference between the detected signal intensity on the ground, assuming a Gaussian beam, compared to an ideal pencil beam, increases with increasing beamwidths for lower elevation angles. Hence, the instrument's performance crucially depends on the optical design to meet the requirements for all possible beam directions.

In a design trade-off, we opted for the choice of cryogenically cooling the feedhorn antenna and front-end, and as such, our system requires a transparent window in our working frequency. An alternative would have been to cool only the LNA, and couple the RF from an ambient temperature feed to the LNA with thermally insulated coaxial or waveguide feed-throughs. However, this would increase the losses, and the result would likely not be much better than an uncooled LNA directly attached to the feed. As such, the window needs to have a minimal reflectivity at the desired frequency and needs to withstand the pressure difference between the interior ($p = 10^{-6}$ Pa) and outside atmospheric conditions. Based on an extensive test campaign of different window materials in a free-space microwave cavity (Speirs et al., 2020; Schröder et al., 2015), we selected ultra-high-molecular-weight polyethylene (UHMWPE) as window material. UHMWPE has a measured dielectric constant of 2.1 and combines low dielectric losses with a relatively low refractive index compared to, e.g., standard high-density polyethylene (HDPE) or PTFE. In addition, UHMWPE has been shown to provide high transmissivity/low emissivity at millimeter wavelengths and favourable mechanical robustness for large vacuum-window applications (D'Alessandro et al., 2018). Recent receiver-window developments further demonstrate that UHMWPE can be precision-machined (e.g., CNC-machined broadband anti-reflection structures) while maintaining very low insertion loss (Joint et al., 2026), and it has been reported to be easier to machine than HDPE in the context of precision receiver optics manufacturing (Yagoubov et al., 2020).

We further reduced the reflectivity of the vacuum window by tuning its thickness to one or multiples of $\lambda/2$ and by applying an additional anti-reflection coating (ARC) on both sides of the window. The ARC layers were designed as quarter-wave coatings with a thickness of $\lambda/4$. At normal incidence, a quarter-wave ARC suppresses reflections by destructive interference between the waves reflected at the air–ARC and ARC–window interfaces, which requires equal reflection amplitudes and a phase difference of π. This condition is fulfilled when the refractive index of the ARC satisfies $n_{\mathrm{ARC}}^2 = n_{\mathrm{air}}\, n_{\mathrm{window}}$. Since $n_{\mathrm{window}} = \sqrt{\varepsilon_r}$ and $n_{\mathrm{air}} \approx 1$, the optimal ARC refractive index becomes $n_{\mathrm{ARC}} = \sqrt{n_{\mathrm{window}}} = \sqrt{\sqrt{\varepsilon_r}}$, (Ulaby et al., 1981).

Figure 4 presents simulations of the window return loss with and without an anti-reflective coating (ARC) for different thicknesses. The results presented were obtained with an ARC thickness of lambda/4, without any geometrical features, and are applied at both top and bottom sides of the window. This is an analytical plane wave expansion centered at 22 GHz (f0 in the plot). At the first reflectivity maxima adjacent to the design frequency, the application of the anti-reflection coating reduces the reflected power by approximately 96 % (corresponding to a reduction of 14.3 dB) compared to the window configurations without ARC. Taking into consideration our effective bandwidth of 200 MHz, the final microwave window will have ARC machined onto it, in accordance with the procedure outlined by Farias et al. (2022). However, most of the presented results in the current work leverage a microwave window without ARC, which turned out to be easier to manufacture for the first

breadboard tests. These tests served mainly for the optimization and characterization of the material properties under vacuum conditions to estimate the behavior of the window due to the pressure difference between the inside and outside of the chamber, and a potential resulting deformation of the material.

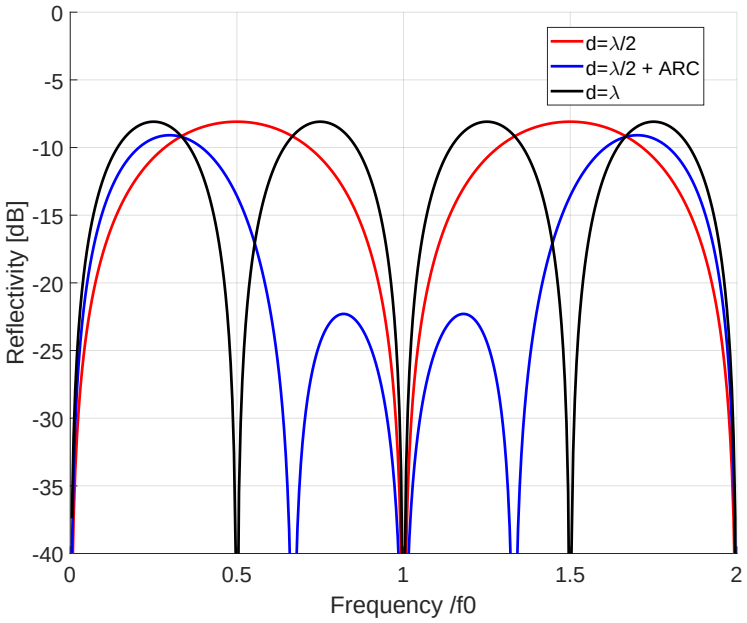

Figure 4. Calculated window return loss in dB for different thicknesses and anti-reflection coating.

Our design of the corrugated horn antenna is based on the work of McKay et al. (2016). The CRYOWARA corrugated antenna, after scaling and modifications, has the shape shown in Figure 5. It has a length of approximately 294.5 mm, an aperture diameter of 67.9 mm, and a square output with a side length of 9.94 mm. The antenna beam propagates along the z-axis with waist w_0 and a diverging beam radius (Goldsmith, 1992). The horn antenna has a w_0 of 15.41 mm and a gain of 20.13 dB with the first sidelobe below -40 dB. A cross-section of the antenna beam pattern is shown in Figure 6, and shows the simulated antenna pattern in the three principal planes relative to the plane of the E-field at the input waveguide. The gain differences are minimal, but there is clearly an increase in the side lobes levels and the cross-polarization. The microwave window results in a slight increase in the first sidelobe level. However, the first sidelobe remains below -35 dB and, thus, stays within the instrument requirements. The window used for the simulations has a 1 lambda, (of the window material) thickness and no ARC.

Outside the cryogenic cooled chamber, we use a 90° off-axis parabolic reflector to focus the atmospheric signal into the feedhorn. The parabolic mirror is designed to keep the spillover below -30 dB. The material is Aluminium 7075 with the focal length located 2.4 mm in front of the horn aperture, where the distance between the antenna and mirror configuration is 342.2 mm. The reflector has an elliptical rim with a major radius of 265.2 mm and a minor radius is 179.4 mm, which

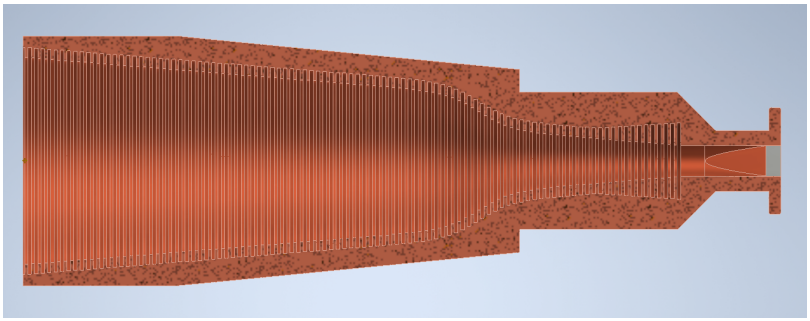

Figure 5. The final design of the corrugated horn showcasing the ultra gaussian profile through a half section of the CAD design.

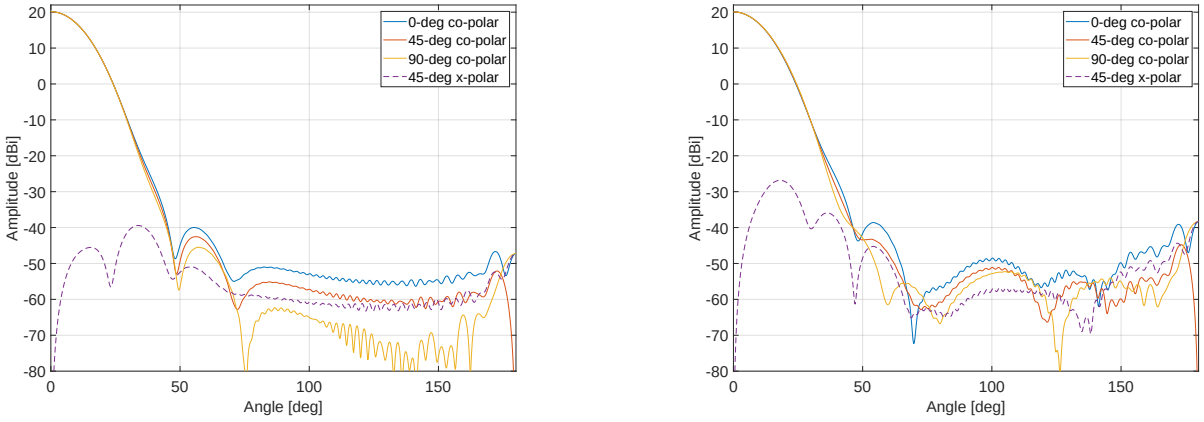

Figure 6. The two plots showcase the difference in the radiation pattern of the horn antenna with, left panel, and without the window, right panel, inserted in the optical path, simulated using CHAMP from TICRA. We compare the radiation at 3 different polarizations: 1) 0 deg, 2) 90 deg, and 3) 45 deg.

was optimised to keep the spillover with the actual feedhorn below -30 dB. The geometry was designed to be lightweight, approximately 2.3 kg, and the center of the rim was moved -30.35 mm to reduce the spillover further due to the beam's divergence. The mirror is mounted on a precision rotation stage from Jenny Science, the ROTAX Rxhq 110-50, which allows a 360 deg rotation and can point the receiver to different elevation angles. The rotation drive is mounted on a linear translation stage again from Jenny Science, the Linax Lxc 80F40, which can be used to change the distance between the mirror and the feed by $\pm\lambda/4$ during or between different measurement cycles in order to reduce the effect of standing waves. As such, the relative power hitting the mirror varies from 99.8% to 99.84%, which is very close to the desired -30 dB spillover corresponding to 99.9% at the scanning mirror. The final antenna-window-scanning mirror configuration has a gain in the far field of 35.6 dBi

shown in Figure 7. A 2D projection of the radiation pattern for co-polar and cross-polar can be found in Figure 8, with the mirror looking at zenith.

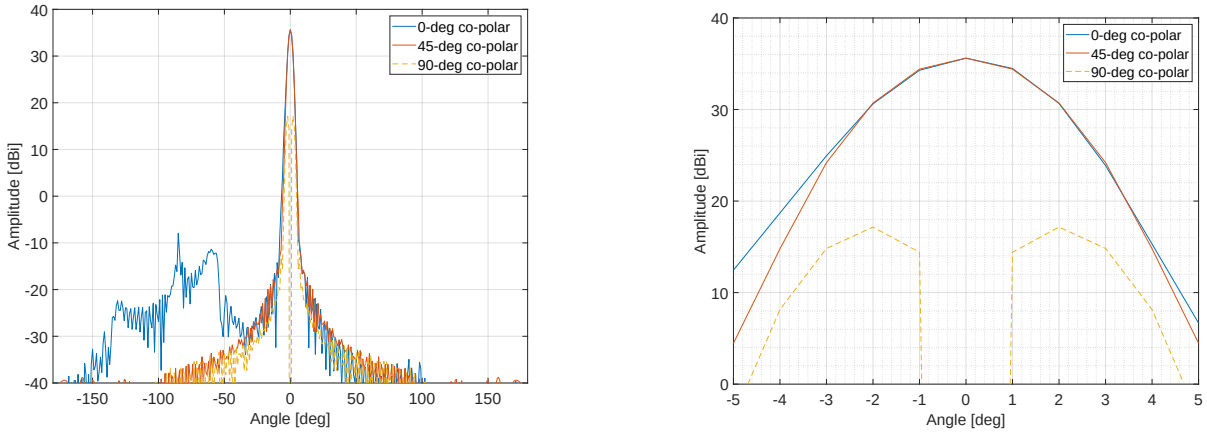

Figure 7. Far-field radiation pattern of the horn–window–mirror configuration (looking at zenith), simulated using GRASP Physical Optics, left panel full angular range, right panel zoomed in.

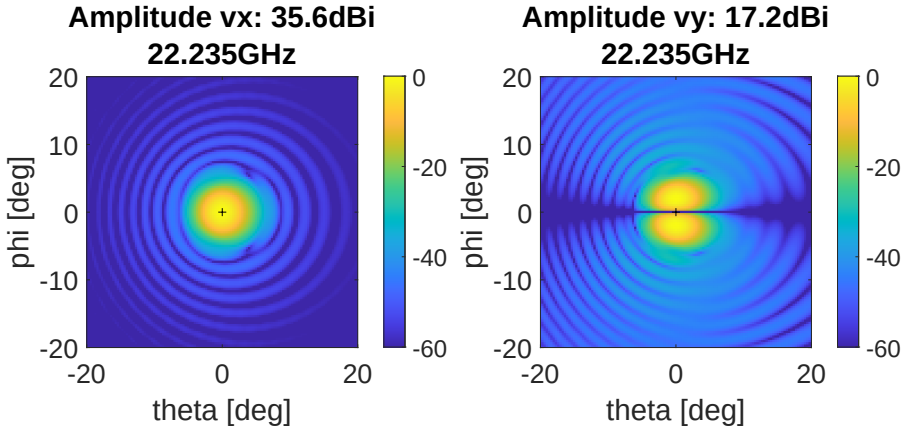

Figure 8. 2D representation of the far field radiation pattern of horn-window-mirror configuration (looking at zenith).

A key goal in the design of the new instrument was the possibility of a remote outdoor deployment for campaigns in the Arctic, Antarctic, or high-alpine environment. CRYOWARA is supposed to be compact and lightweight to be easily deployed onto measurement platforms or high-altitude research stations. Therefore, the design of a weather-proof housing and climate control of the main instrument parts are important. In particular, the cooling power of the cryocooler has to be well-dimensioned to provide sufficient cooling under extreme weather conditions. The entire instrument is going to be weatherproofed from rain,

snow, or other precipitation through an automated rain hood cover that closes and protects the reflector and calibration targets. In the meantime, the receiver will always be in a fixed and temperature-controlled housing. We have also added counterweights to ensure a better balance of the entire mirror mounting concerning the center of gravity relative to the rotation stage.

2.2 The vacuum chamber

Cryogenic cooled front-ends were more common for astronomical radio telescopes, e.g., the Atacama Large Millimeter Array (ALMA) (Yagoubov et al., 2020). The advantage of cryogenically cooled instruments is their reduced noise level and, thus, increased sensitivity, decreasing the required integration time to reach the necessary noise level for a profile inversion. This is achieved by housing the feedhorn and all front-end electronics such as the low-noise amplifiers (LNA), the orthomode transducer (OMT), the cryocooler cold finger, the turbo pump flanges, and all mountings in the vacuum chamber. The vacuum chamber of CRYOWARA is designed to be as compact as possible in order to minimize its volume and overall system complexity compared to existing cryogenic water vapor radiometers (Hallgren et al., 2013). In the system described by Hallgren et al. (2013), the instrument includes temperature-tunable internal hot and cold calibration loads housed inside the vacuum chamber. While this approach provides highly stable and well-controlled calibration reference temperatures, it requires a significantly larger vacuum chamber as well as additional thermal interfaces and cooling power. In contrast, CRYOWARA is designed for outdoor operation and therefore employs an ambient hot load and the atmosphere as a cold calibration reference. This design choice allows for a substantially more compact vacuum chamber and reduces the required cryocooler power, at the expense of increased sensitivity to environmental conditions and the need for careful monitoring of ambient temperature and atmospheric stability. The trade-off between internal calibration loads and external reference loads thus reflects a balance between calibration stability and system complexity, which is driven by the intended deployment environment of the instrument. Figure 9 presents a CAD scheme of the vacuum chamber and its interior.

The cryocooler is the most critical part of the system as it controls the temperature of the LNAs. The lower the temperature, the lower the losses in the receiver chain (front end), and as a result, the lower the receiver noise temperature. We choose to use an AMETEK Stirling cooler due to its compact size, low power consumption e.g., 240 W, and mean time of failure 22 years as specified by the manufacturer. The cooler is connected through a flange from underneath the vacuum chamber. The balancer is located at the lower edge of the scheme. Minimizing the size of the vacuum chamber and reducing the thermal conductance are essential for reaching the coldest possible temperatures at the cold finger of the cryocooler. The LNAs are directly connected through copper braids with the cold finger to ensure efficient cooling.

Figure 10 shows the copper braids, which are designed so that both LNAs receive the same cooling power from the cold finger. The copper braids that connect the cold head of the cryocooler to the LNAs have an estimated conductance per strap of approximately 0.785 W/K @ 40 K(as stated by the manufacturer). Attached to the LNAs is the orthomode transducer that can be seen in Figure 11. The ortho-mode transducer is designed with a square waveguide input matching the corrugated antenna and has a WR42 output waveguide for dual-polarization measurements. The simulated reflectivity of the OMT is for all ports at 22.235 GHz below -27 dB. The LNAs at 22.235 GHz have a measured gain of approximately 34 dB at 296 K and approximately 32 dB at 4 K. The S11 in both cases, it remains below -20 dB.

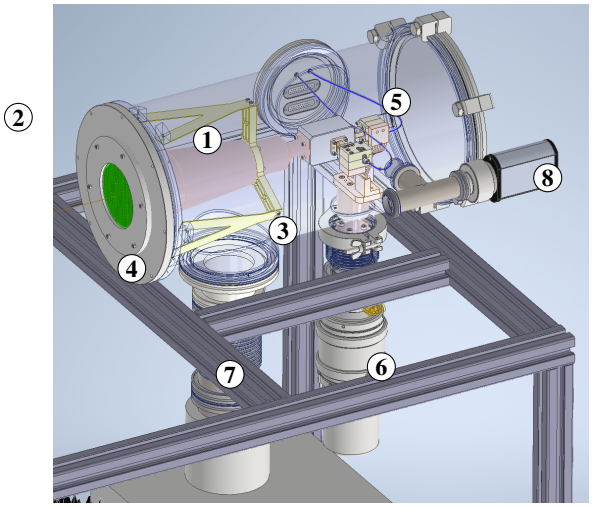

Figure 9. 3D model of the vacuum chamber, with a length of 483 mm and an external diameter of 240 mm, showing the main components: **1)** Corrugated horn, **2)** Window, **3)** Vacuum chamber, **4)** Horn mounting structure, **5)** OMT-LNAs, **6)** Cold head (cryocooler), **7)** Vacuum pump, **8)** Pressure gauge.

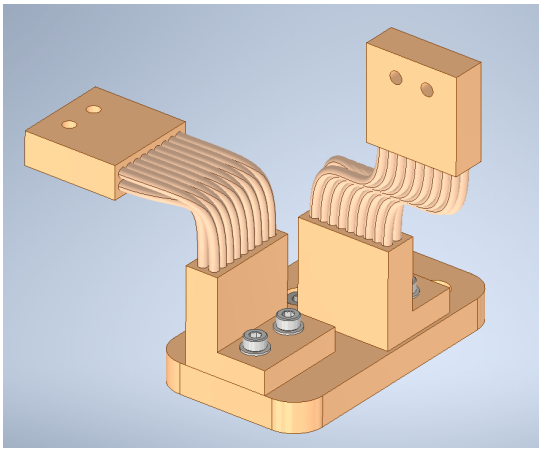

Figure 10. 3D model of the copper braids. Each attaches to the LNAs to transfer the heat on the cold head and cool them down.

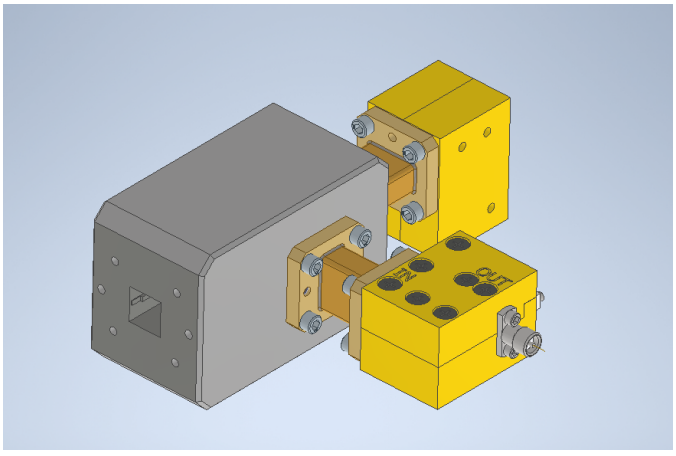

Figure 11. 3D model of OMT, waveguide extension and LNAs. The OMT is used to split the square input into 2 orthogonal polarizations, horizontal and vertical.

The feed horn, OMT, and LNAs are mounted in the vacuum chamber with a thermally insulating structure, which is machined from the fiberglass and resin composite material G10. The specific material used is HGW 2372, and the geometry was designed to ensure a high stiffness of the support structure and to minimise misalignment by thermal contraction of the material when cooled. The design of the vacuum chamber, supporting structure, and cryocooler choice is based on thermal analysis using the

ANSYS software, assuming a minimum load, the cooler has to remove. A simplified model of the vacuum chamber was used to characterize the heat conductance into the vacuum chamber. Table 2 shows a summary of the material and boundary conditions. To ensure that we can reach a temperature of at least 55 K in the area of the LNAs, we apply a 50 K constant temperature on the simplified model of the mounting surface of the cold head of the cryocooler. In addition, the environment (represented by a sphere that surrounds the whole cryostat) radiates heat at 295 K (radiation is considered perfect between components, and nothing is lost to the surroundings). All contacts are considered bonded without friction taken into account. This results in a temperature at the center of the optical window of 297 K. The estimated heat load that the cryocooler should remove is approximately 10 W. The AMETEK cryocooler is specified to reach 77 K at the cold finger with a heat load of 17.5 W. Figure 12 visualizes our simulation results and the thermal gradients inside the chamber. The ANSYS simulation indicates that the feedhorn, LNAs, and OMT can be cooled down to about 50 to 60 K while the cooler is removing a heat load of 10 W. The thermal load from the walls of the vacuum chamber can be further reduced by wrapping all hardware inside the chamber with a highly reflective material, such as MLI, to reflect the thermal radiation emitted by the walls. For the breadboard set-up we have not used MLI, and this is something that will be implemented in the final assembly.

Table 2. Material parameters used for the thermal simulations in ANSYS.

Component	Material	Emissivity	Thermal Resistance, at 300 K	Boundary Condition
Environment	Air	1	3.6e-3 K/W	295.15 K, radiation
Vacuum chamber	Stainless Steel	0.35	7.7e-4 K/W	Conduction, Radiation
Corrugated antenna	Gold plated Cu	0.3	2.1e-4 K/W	Conduction, Radiation
Supporting structure	Fiber Glass	0.9	6.7e-2 K/W	Conduction, Radiation
LNAs	Aluminium single block	0.1	4.2e-2 K/W	Conduction, Radiation
Copper Braids	Copper	0.2	2.3e-3 K/W	Conduction, Radiation
Cooler flange	Copper	0.2	2.6e-4 K/W	60 K, Conduction, Radiation
OMT	Aluminium	0.1	1.6e-2 K/W	Conduction, Radiation
Optical Window	Polyethylene	0.9	0.684 K/W	Conduction, Radiation
Optical Flange	Stainless Steel	0.35	1.9e-3 K/W	Conduction, Radiation

3 Comparison with MIAWARA

MIAWARA was designed with a simplistic approach, reliability, and performance in 2002, as the main goals. The design was focused on a reliable instrument that can operate autonomously without human intervention. As such, it has been successful for measuring water vapor time series (Bell and Murk, 2023; Bell et al., 2025). It has also successfully participated in campaigns for inter-comparison with similar radiometers Deuber et al. (2005). The design is based on a flat reflector with an optimized Gaussian beam shape, and an edge taper of 45.9 dB. Accompanied by a conical corrugated antenna with a FWHM of 6^o. CRYOWARA, on the other hand, as described in the previous section, has a parabolic reflector with an edge taper of 30 dB

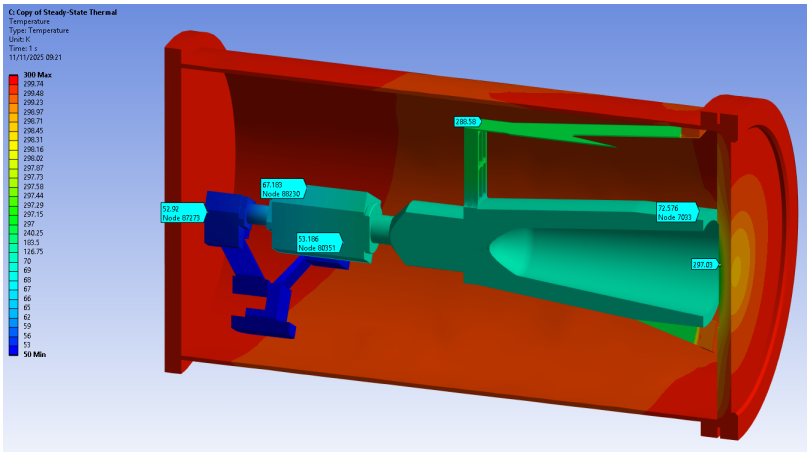

Figure 12. Simulated temperature distribution in the vacuum chamber with a 60 K constant temperature on the OMT. This simplified model is used to determine the temperature of the cryocooler due to the load.

and a profiled corrugated antenna with FWHM of 3^o. Due to the parabolic reflector, the beam is collimated, and we can reduce the size of the reflector, as such keeping the size of the instrument as small as possible. This allows us to achieve a far-field gain of 35.6 dBi. On the other hand, MIAWARA's gain is at 30.1 dBi, but to achieve so, it requires a 90 cm long horn antenna with an aperture of 20 cm. The two instruments are quite similar in terms of gain performance, but CRYOWARA, as we described in 2, has a slightly higher gain and a much more compact design. Though the main advantage of the new radiometer is the CRYOGENIC front-end. As it will be described in the later results section, 5, the system noise temperature lies somewhere between 40-50 K, whereas for MIAWARA the noise temperature is in the range of 130-140 K. Furthermore, the reduced noise impacts the temporal resolution of the retrieved water vapor profiles. During nominal operation of MIAWARA, we retrieve water profiles every 6-12 hours, but to achieve higher altitude coverage, the operational data is integrated over 24 hours. Typically MIAWARA retrieves water vapor profiles on about 80% of the days per year. Already, the breadboard setup of CRYOWARA permitted the retrieval of water vapor profiles with integration times of 2 hours. This shorter integration time should also allow the retrieval of water vapor profiles on days when atmospheric conditions are not optimal throughout the day, e.g., even during precipitation gaps. The final main difference is the dual polarization of CRYOWARA, compared to the single polarization measurements of MIAWARA, further improving the signal-to-noise ratio for the new instrument. In Table 3, we present the whole comparison between the two instruments to outline the performance difference between both instruments.

4 Calibration

To minimize gain non-linearities in the CRYOWARA system, the calibration strategy is based on measuring and calibrating a *signal difference* rather than absolute brightness temperatures. This difference is then scaled to an equivalent *zenith brightness temperature*. Two well-established methods are used to achieve this:

Table 3. Comparison of key Parameters for MIAWARA and CRYOWARA

Parameter	MIAWARA	CRYOWARA
Calibration technique	Balanced calibration	Balanced calibration or frequency switch
Operational mode	Single sideband mode, single polarization	Single sideband mode, dual polarization
RF amplification	2 uncooled HEMT amplifiers (gain 35 dB each; noise figure 1.49/1.85 dB; Miteq AMFWW series)	2 cooled LNAs (gain 28 dB each at 5 K; noise figure 0.12 dB; Low Noise Factory)
Mirror	Plane mirror (Gaussian-beam optimised); edge taper $= 45.9$ dB, far field gain 30.1 dB	Parabolic mirror (Spillover optimised); edge taper $= 30$ dB, far field gain 35.6 dB
Antenna	Conical corrugated horn, single polarization ($\theta_{\mathrm{FWHM}} \approx 6^\circ$)	Profiled corrugated horn, dual polarization, square waveguide output 9.94 mm^2, ($\theta_{\mathrm{FWHM}} \approx 3^\circ$; in the far field including the reflector)
Receiver noise temperature	135 K (SSB)	45 K (SSB)
Radio-frequency range	21.735–22.735 GHz	22.135–22.335 GHz
Spectral analysis	Until 2024: AC-240 FFT spectrometer (1 GHz bandwidth); 16384 channels; 61 kHz resolution per channel, after 2024 USRP X310 and AC-240 FFT side by side	USRP X310 Software Defined Radio receiver (200 MHz bandwidth); 16384x2 channels; 12.2 KHz resolution per channel

1. **Balancing Calibration:** This approach calibrates the signal difference between the sky viewed at a low elevation angle and near-zenith angle. The near-zenith view includes a partial view of a microwave absorber, chosen so that the continuum brightness temperature closely matches the low-elevation sky signal. This calibration scheme helps to isolate and stabilize gain-related effects, Deuber et al. (2004b), Parrish et al. (1988).

2. **Frequency Switching:** In this method, the local oscillator (LO) is switched between two nearby frequencies. The choice of frequency offset is a trade-off between a small offset, which reduces information content in the lower stratosphere, and a large offset, which increases instrumental artifacts arising from the frequency dependence of the front-end. The resulting signal difference between these two frequencies, in terms of counts, is transformed into a brightness temperature (described below). This method mitigates system gain instabilities, Forkman et al. (2016). The resulting signal will have both a negative and a positive peak with a frequency domain separation equal to two times the frequency switch.

Both calibration methods require reference views of known brightness temperatures:

– The *hot reference* is provided by a microwave absorber at a known environmental temperature.

– The *cold reference* is the sky at a high elevation angle. Its brightness temperature is estimated using a *tipping curve calibration*, performed every 15 minutes. This involves measuring the sky brightness temperature at various elevation angles to estimate the *tropospheric opacity* τ, which affects how the sky signal is attenuated, 2. The cosmic background radiation T_0 is also accounted for in this model.

Independent of whether we use frequency switching or the reference absorber, we record the difference in signal according to Equation 1.

$$\Delta T_{sky} = \frac{\Delta P}{P_{load} - P_{sky}} (T_{load} - T_{sky}) \tag{1}$$

where ΔT_{sky} is the difference in brightness temperature and ΔP is the difference in the measured power, either at the two frequencies for the frequency switch calibration or the difference in measured power for the 2 different signals, e.g, reference absorber or atmospheric signal. T_{sky} and P_{sky} are the cold sky brightness temperature and corresponding counts, respectively.

Both options have advantages and disadvantages. One key drawback of the balancing approach is that, by using the reference absorber along the optical path, we are losing integration time when we are observing 50% of the time at the reference position. With frequency switching, the line of interest is observed all the time, and we should have sqrt(2) better SNR than with the balancing calibration. Another issue that arises in the balancing calibration is the generation of standing waves: moderately reflecting bodies near the antenna can introduce systematic baseline errors on the calibrated spectra if not properly mitigated. On the other hand, the frequency switch has been documented as being used only for the retrieval of relatively narrow atmospheric emission lines, such as the 110 GHz O3 and 115 GHz CO line Forkman et al. (2016) and (Wang et al., 2025). Since the 22.235 GHz water-vapor line is intrinsically broader, a substantially larger frequency offset is needed to reach the line wings far enough from the peak, yet still maintain comparable signal intensity to the center, making this approach less common for broader lines. In order to verify the frequency switching approach, we have performed preliminary tests as discussed in section 5.

4.1 Tipping curve calibration

The tipping curve calibration provides a reliable estimate under clear sky conditions of the effective cold sky temperature, which is essential for ensuring that the signal difference can be accurately scaled to a physical brightness temperature. The cold sky temperature is calculated according to equation 2.

$$T_{cold,sky} = T_0 e^{-\tau/sin\theta} + T_{trop}(1 - e^{-\tau/sin\theta}). \tag{2}$$

For ground-based radiometers dedicated to measuring the narrow spectral line in the stratosphere and mesosphere, the tropospheric signal is often not directly retrievable due to the limited bandwidth of the high-resolution spectrometer. The tropospheric opacity is estimated from a tipping curve and included in the baseline subtraction. By assuming a single-layer

troposphere with a mean temperature T_{trop}, the signal T_{B} from the middle atmosphere is attenuated by the troposphere according to Equation 3

$$T_{b,ground(f)} = T_B(f)e^{-A\tau(f)} + T_{trop}(1 - e^{-\tau/sin\theta}). \tag{3}$$

where A is the airmass factor, the elevation angle θ. The airmass factor is given by Equation 4 according to Deuber et al. (2004b),

$$A = \frac{1 + z/R}{\sqrt{\sin^2\theta + \frac{2z}{R} + \frac{z^2}{R^2}}} \tag{4}$$

where R is the radius of the Earth and z is the thickness of a thin atmospheric layer (e.g., the troposphere). Except for very low elevation angles, the following approximation for A is valid (less than 1% difference for $\theta > 20^o$):

$$A = \frac{1}{sin\theta} \tag{5}$$

T_{trop} is estimated from the ambient temperature of the ground T_{ground} according to Deuber et al. (2004b),

$$T_{trop}(f) = c_1(f)T_{ground} + c_0(f) \tag{6}$$

In Equation 6, c1 and c0 are linear regression coefficients for different elevation angles and frequencies. For 22.235 GHz, c0 is in the range of 266.3–266.9 K, and c1 is 0.690–0.752, depending on the elevation angle. With this technique, T_{trop} can be estimated with a standard error of 3.7–3.9 K. For the tropospheric opacity τ, we need at least two measurements at different elevation angles.

To avoid the need for a permanent installation of liquid nitrogen reservoir for the cold load calibration, we will be using the sky at an elevation angle of approximately 60° (the same angle is used for MIAWARA Deuber et al. (2004b)). The value is occasionally validated against an external liquid nitrogen calibration, and in combination with the hot target, which can be used when the rotating mirror looks at nadir, we obtain the appropriate hot-cold calibration.

5 Preliminary results using a breadboard test setup

In this section, we present the first results of the initial tests during the development and integration phase of the radiometer. The cryocooler has undergone some tests to confirm the temperature range that can be achieved during operation. The test setup can be seen in Figure 13. The cooler can work at 250 W input power, and we benchmarked the performance under full power in a vacuum of 10^{-6} mbar. We were able to reach a temperature of 30 K without any external heat load attached to the

cold head. We are currently finalizing the integration of the cryocooler in the vacuum chamber of CRYOWARA, as shown in Figure 14. When tested in the chamber and presented in Figure 14 with all components installed inside, the cold head reached a temperature of 46 K without any additional heat load, except the thermal radiation emitted from the walls of the vacuum chamber.

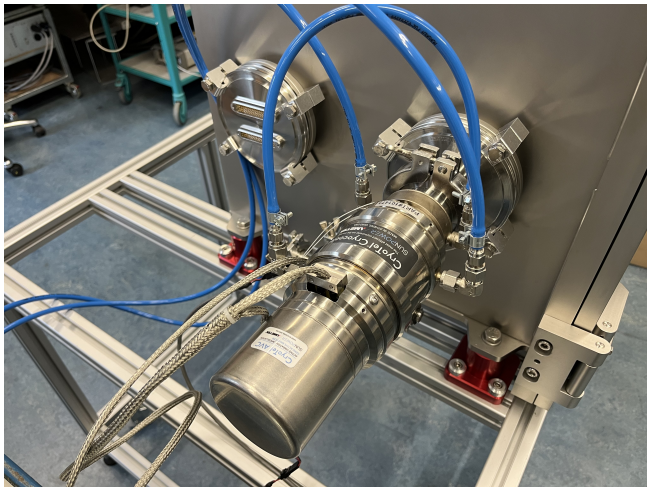

Figure 13. First test to determine the cryocooler performance under different scenarios a) no heat load attached on the cold head, b) dummy mass attached to evaluate the temperature distribution.

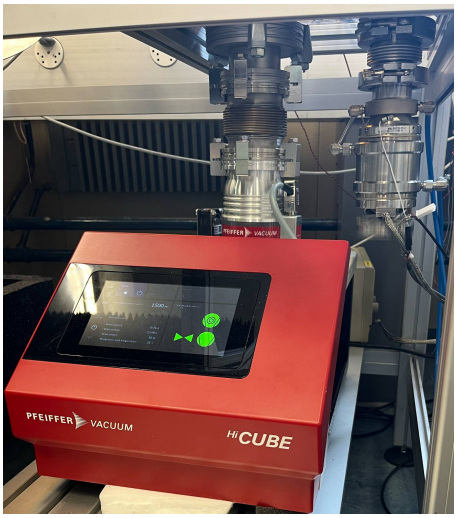

Figure 14. Final integration of the cryocooler on the vacuum chamber, next to the pumping station.

Furthermore, we had to evaluate how the cryocooler interacts with the other components inside the vacuum chamber. Therefore, we validated the performance of the corrugated horn antenna with the OMT regarding the return loss (dB). We measured different S11 and S22 parameters at the different ports with the use of a Vector Network Analyser (VNA). Two tests were performed: 1) an aluminium plate was used at the aperture of the antenna, and 2) a black body absorber covered the whole aperture. The return loss in both cases was measured and is visualized in Figure 15. These measurements characterize the performance of the OMT and corrugated antenna.

We quantified the return loss of the window material without the ARC, when placed at the aperture of the horn OMT configuration Figure 16, for 0.5 and 1 lambda (of the material) thickness. We see that the null is not perfectly at 22.235 GHz. The reasons for the offset appear to be related to the window not being machined to the exact theoretical thickness of 4.45 mm for 0.5 lambda and 8.89 mm for 1 lambda.

The next step was to simulate the performance of the radiometer using a model atmosphere to predict the expected line shape. This was achieved with the use of ARTS (Buehler et al.). We used a clear sky atmosphere and placed our sensor at mid-latitudes in the wintertime, pointing at a zenith angle of 45 degrees. The expected shape of the line can be seen in Figure 18, where it is compared with the first calibrated data. The peak of brightness temperature for a 1D atmosphere, clear sky radiance is around 21 K. We simulated as well the performance of the frequency switch calibration mentioned in Section 4.

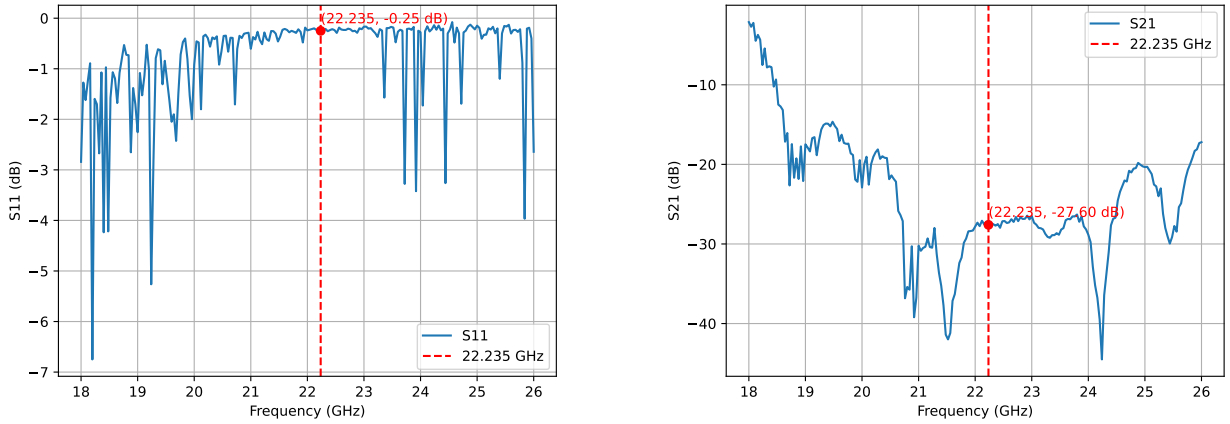

Figure 15. Measured return loss of the horn and OMT configuration over a) an aluminium plate right on the aperture, b) a pyramidal absorber.

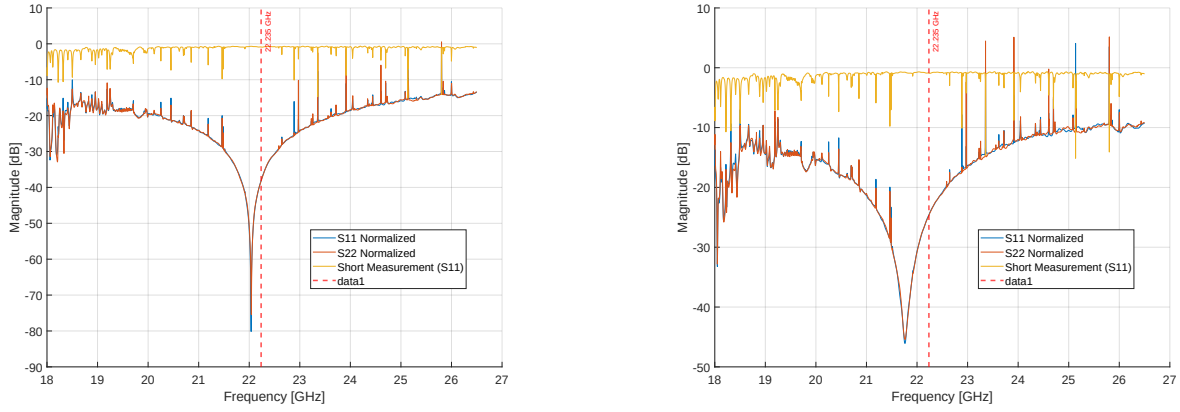

Figure 16. Measured return loss of 2 microwave windows using a vector network analyzer (VNA): a) 0.5 lambda thickness, b) 1 lambda thickness.

Figure 17 shows a shift from the center of $\pm$ 10 MHz while the difference in brightness temperature is approximately 0.4 K. The results are compared to the first measurements with the breadboard from the laboratory.

For the test, we utilized the spectrometer USRP x310. We performed a hot-cold calibration using liquid nitrogen as the cold target and a hot load located inside the radiometer to calibrate the instrument and calculate T_{sky}. Using the counts' output (equivalent to raw voltage or power output) from the USRP, we averaged over the 16384 channels, using equation 1 and extracted the measured ΔTB. The resulting calibrated spectra clearly show the line with an approximate temperature difference of 1 K.

The first results obtained with the breadboard set-up already indicate the performance gain of a cryogenically cooled instrument

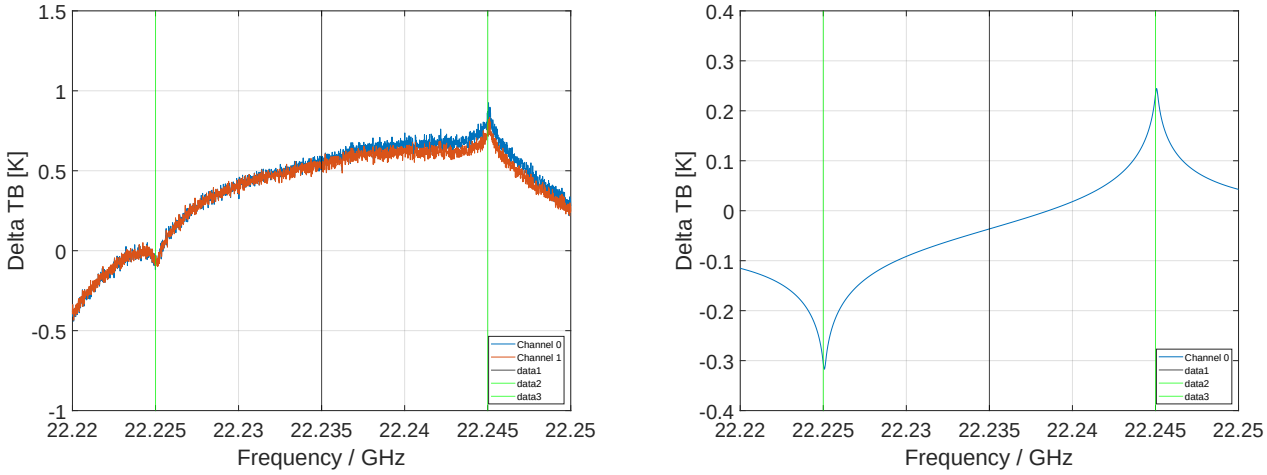

Figure 17. The two plots show calibrated and simulated spectra using a frequency switch calibration, a) Calibrated spectra testing the frequency calibration, with a 10 MHz switch in frequency from the center line, b) Line-by-line radiative transfer simulation using frequency switch, for clear-sky conditions at mid-latitude in winter, using ARTS.

for retrievals of water vapor profiles. Furthermore, we performed experiments with the uncooled instrument, leveraging a hot-cold calibration using liquid nitrogen at nadir and an ambient target at room temperature, and no microwave window in front of the horn aperture to compare the performance differences. Measurements were made at a zenith angle of 45°as shown in Figure 1. The integration of the measurements is approximately 5 hours, and was recorded on the 17th of February 2025.

Both polarizations show a very good agreement with the simulated data, Figure 18. We assumed clear sky conditions, with the same elevation angle, altitude, and mid-latitude in winter-time conditions. To match the peak of the spectral line, the simulated line was increased by 0.4 K. The amplitude of the line is 0.45 K with a noise level of 0.04 K, confirming that we are actually measuring the atmospheric signal. To calculate the receiver noise temperature (T_{REC}), the most common approach is to calculate the y-factor, from the physical temperatures T_{HOT} and T_{COLD} of two calibration targets, from Equation 7 (Deuber et al., 2004b). The receiver noise temperature was measured close to 125 and 140 K, respectively, for the two polarizations and is shown in Figure 19.

We performed the same measurements with the cooled instrument as well, but this time for a lower elevation angle of 30°. The measurements were performed on the 15th of May. The cold head temperature was at 51.5 K. The resulting T_{rec} for both polarizations can be seen in Figure 19. The value of approximately 45 K shows a clear improvement in the receiver noise temperature for the cooled instrument compared to the uncooled. The difference in the brightness temperature absolute values relates to the atmospheric conditions and elevation angle. The measurements were performed in February and May, respectively, were the atmospheric conditions were different, as well as the elevation angles of 45 and 30 degrees. A lower elevation angle results in a longer sounding path through the atmosphere, which results in an increased brightness temperature. In addition, we notice a slight difference between the two polarizations of the cooled data, which is related to the geometric

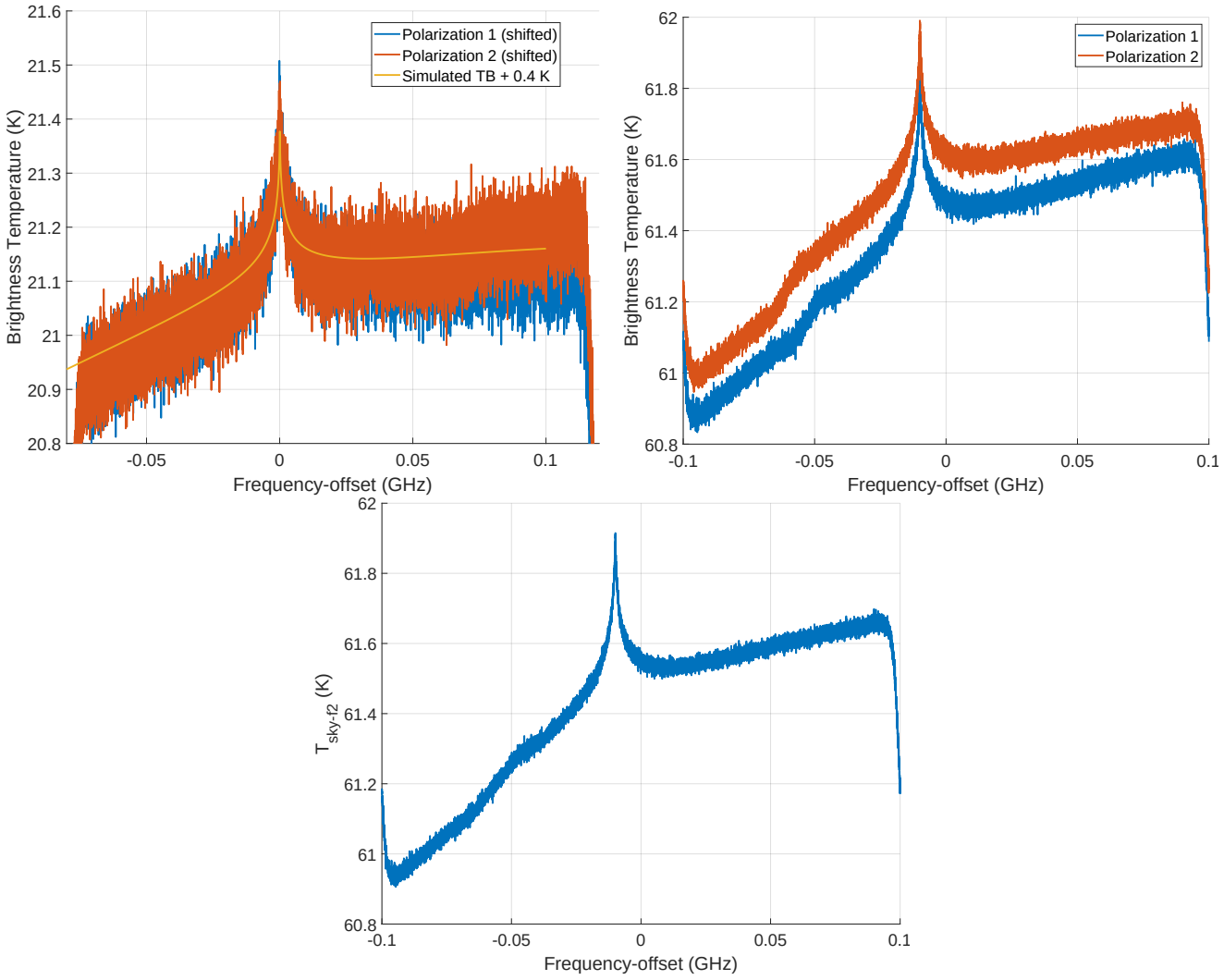

Figure 18. First results with the breadboard set up: Left panel: Calibrated brightness temperature using LN2 as the cold target over a 5-hour integration time vs simulated profile without the cryocooler, right panel: Calibrated brightness temperature using LN2 as the cold target over a 5-hour integration with the cryocooler, bottom panel: the average of the two polarizations from right panel, where the noise per measurement is reduced from 0.405 K to 0.286 K by averaging the two polarizations (factor $\sqrt{2}$).

setup inside the vacuum chamber, as polarization one is about 4 K cooler than polarization 2. The spectral noise per measurement for each polarization is 0.402 K and 0.407 K respectively. The average of the polarization is shown in 18 in panel c). The noise is reduced by a factor of $\sqrt{2}$, resulting in 0.286 K. It should also be mentioned the area around -50 MHz where a jump in the spectra of both polarizations appears. We suspect that this is due to some internal reflections in the front end. The source has not yet been identified but we plan to perform antenna measurements in the future and address this issue. The spectrometer has a DC channel right in the middle of the 16384*2 channels. This results in the spectral lines being shifted by 0.02 GHz in

the 200 MHz bandwidth. To match the simulated spectra in ARTS, the uncooled data were shifted in frequency by 20 MHz to align the peaks.

$$T_{\mathrm{REC}} = \frac{T_{\mathrm{HOT}} - yT_{\mathrm{COLD}}}{y-1} \tag{7}$$

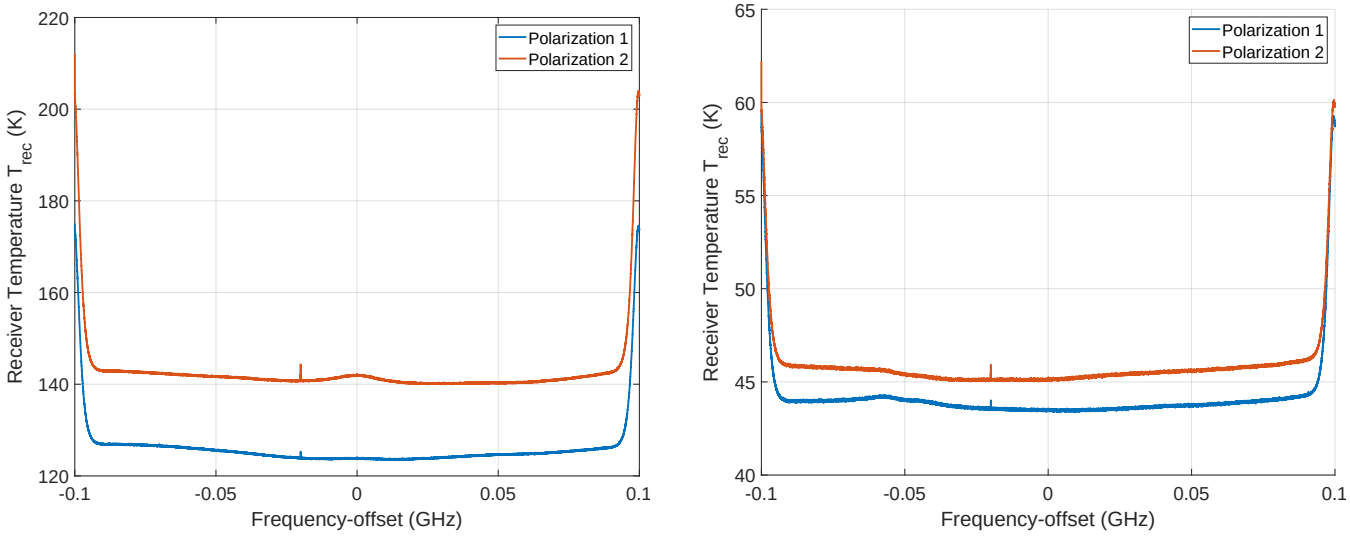

Figure 19. Receiver noise temperature measurements using LN_2 calibration: (a)Receiver noise temperature of the uncooled system measured during a hot-cold calibration using LN_2, (b) Receiver noise temperature of the cooled system measured during a hot-cold calibration using LN_2.

6 Discussion

The first results obtained with the breadboard radiometer confirm the design specification of the quasi-optical components and show a reduction of the receiver noise temperature while using the cryocooler. The receiver noise temperature of 45 K, compared to the MIAWARA receiver noise temperature of 120–140 K, reduces the system-noise contribution by roughly 63–68%, which in turn lowers the measurement error by almost the same factor $\left(\Delta T \propto T_{\mathrm{sys}}/\sqrt{B\tau}\right)$. Practically, this means that the same measurement noise can be achieved with shorter integration time, permitting the study of faster processes in the atmosphere, altering the water vapor volume mixing ratio, for instance, the diurnal variation of the stratospheric /lower mesospheric water vapor, as with a reduced sampling time per spectrum, rapid-event case studies become feasible without sacrificing accuracy.

Our laboratory tests already demonstrate that the radiometer can detect the weak atmospheric signal of the water vapor line at 22 GHz, and the instrument performance will improve further when the instrument is integrated into the outdoor weather-proofed housing. Currently, the atmospheric soundings are affected by the laboratory environment, offering only a limited view

of the sky, reducing the elevation angles for the beam pointing. The next steps are to finalize the assembly of the radiometer and to deploy the instrument outside to perform an environmental test evaluating the instrument stability and climatization, and to retrieve a first continuous water vapor time series.

Furthermore, we conducted a long-term stability test for the cooled and vacuum-pumped instrument. The LNA's temperature, as well as the entire receiver chain, started to reach a plateau and remain stable after a week of continuous operation. A first guess for this behavior is that outgassing from water vapor that remains in the chamber due to the assembly of the receiver chain under normal laboratory conditions resulted in some drift of the LNAs and receiver noise temperature during the first days after initializing the vacuum chamber and starting the cooler. The leakage of the vacuum chamber is negligible and was tested with Helium, essentially reducing the power uptake to the turbopump, which only runs at a moderate power to sustain a pressure of 1.6×10^{-6} mbar in the chamber.

7 Conclusions

This study presents initial results of a breadboard radiometer, CRYOWARA, to observe the water vapor line at 22.235 GHz. The instrument is designed as a next-generation ground-based water vapor sensor covering the entire middle atmosphere and will replace the existing and aged MIAWARA in a few years. The new instrument consists of a cryogenically cooled dual polarization receiver chain and corrugated feedhorn with sidelobes below -30 dB packed within a vacuum chamber. Furthermore, CRYOWARA contains a linear stage moving the parabolic primary mirror, reducing standing waves. The parabolic mirror is designed to achieve a FWHM beamwidth of 3° with a spillover close to -30 dB.

Preliminary results comparing the cooled and uncooled receiver chain indicate a reduction of the receiver noise temperature from 140 K to about 50-60 K. Furthermore, we performed LN2 calibrations and tested tipping curve calibrations for both the cooled and uncooled measurements, indicating good agreement with the simulations conducted with the ARTS radiative transfer model. The differences in brightness temperature between the measured spectra and ARTS were in the range of 0.4 K. Furthermore, we demonstrate simulations and first measurements leveraging the frequency switching calibration with the cooled receiver chain, opening a pathway to avoid the balancing calibration during nominal operation when CRYOWARA will be deployed at the Zimmerwald observatory.

Author contribution

AF performed the quasi-optical and overall design of CRYOWARA as well as the data analysis of the various tests with contribution and guidance from AM and GS. AB provided valuable support in the radiative transfer calculations and calibration. The manuscript was written by AF with edits from all authors.

Acknowledgements

Gunter Stober, Axel Murk, Alistair Bell, and Adrianos Filinis are members of the Oeschger Center for Climate Change Research. This work had been completed as part of the "Swiss H_2O Hub for High-quality water vapor measurements from ground to space" project financed by GCOS Switzerland (https://www.meteoswiss.admin.ch/about-us/research-and-cooperation/programme gaw-ch-and-gcos-ch/gaw-ch-and-gcos-ch-supported-activities.html). The authors thank the ARTS developers for their continued work with the radiative transfer software and user support. We acknowledge the technical support from AMETEK to integrate the Cryocooler into the vacuum chamber.

References

Andrews, D., Holton, J., and Leovy, C.: Middle Atmosphere Dynamics, International Geophysics, Elsevier Science, 1987.

Bell, A. and Murk, A.: Monitoring of Middle Atmospheric Water Vapour, 2023.

Bell, A., Sauvageat, E., Stober, G., Hocke, K., and Murk, A.: Developments on a 22 GHz microwave radiometer and reprocessing of 13-year time series for water vapour studies, Atmospheric Measurement Techniques, 18, 555–567, https://doi.org/10.5194/amt-18-555-2025, 2025.

Brasseur, G. P. and Solomon, S.: Aeronomy of the middle atmosphere: Chemistry and physics of the stratosphere and mesosphere, vol. 32, Springer Science & Business Media, 2005.

Buehler, S. A., Larsson, R., Lemke, O., Pfreundschuh, S., Brath, M., Adams, I., Fox, S., Roemer, F. E., Czarnecki, P., and Eriksson, P.: The Atmospheric Radiative Transfer Simulator Arts, Version 2.6—Deep Python Integration.

Carr, J. L., Horváth, A., Wu, D. L., and Friberg, M. D.: Stereo Plume Height and Motion Retrievals for the Record-Setting Hunga Tonga-Hunga Ha'apai Eruption of 15 January 2022, Geophysical Research Letters, 49, e2022GL098 131, https://doi.org/10.1029/2022GL098131, 2022.

De Wachter, E., Hocke, K., Flury, T., Scheiben, D., Kämpfer, N., Ka, S., and Oh, J. J.: Signatures of the Sudden Stratospheric Warming events of January–February 2008 in Seoul, S. Korea, Advances in Space Research, 48, 1631–1637, https://doi.org/https://doi.org/10.1016/j.asr.2011.08.002, 2011.

Deuber, B., Kampfer, N., and Feist, D.: A new 22-GHz radiometer for middle atmospheric water vapor profile measurements, IEEE Transactions on Geoscience and Remote Sensing, 42, 974–984, https://doi.org/10.1109/TGRS.2004.825581, 2004a.

Deuber, B., Kampfer, N., and Feist, D. G.: A new 22-GHz radiometer for middle atmospheric water vapor profile measurements, IEEE Transactions on Geoscience and Remote Sensing, 42, 974–984, 2004b.

Deuber, B., Haefele, A., Feist, D. G., Martin, L., Kämpfer, N., Nedoluha, G. E., Yushkov, V., Khaykin, S., Kivi, R., and Vömel, H.: Middle Atmospheric Water Vapour Radiometer (MIAWARA): Validation and first results of the LAPBIAT Upper Tropospheric Lower Stratospheric Water Vapour Validation Project (LAUTLOS-WAVVAP) campaign, Journal of Geophysical Research: Atmospheres, 110, 2005.

D'Alessandro, G., Paiella, A., Coppolecchia, A., Castellano, M., Colantoni, I., de Bernardis, P., Lamagna, L., and Masi, S.: Ultra high molecular weight polyethylene: optical features at millimeter wavelengths, Infrared Physics & Technology, 90, 59–65, 2018.

Farias, N., Beckman, S., Lee, A., and Suzuki, A.: Simulated Performance of Laser-Machined Metamaterial Anti-reflection Coatings, Journal of low temperature physics, 209, 1232–1241, 2022.

Federal Office of Meteorology and Climatology MeteoSwiss: GAW-CH and GCOS-CH Supported Activities, https://www.meteoswiss.admin.ch/about-us/research-and-cooperation/programmes-gaw-ch-and-gcos-ch/gaw-ch-and-gcos-ch-supported-activities.html, accessed 2025-10-28.

Forkman, P., Eriksson, P., and Winnberg, A.: The 22 ghz radio-aeronomy receiver at onsala space observatory, Journal of Quantitative Spectroscopy and Radiative Transfer, 77, 23–42, 2003.

Forkman, P., Christensen, O., Eriksson, P., Billade, B., Vassilev, V., and Shulga, V.: A compact receiver system for simultaneous measurements of mesospheric CO and O 3, Geoscientific Instrumentation, Methods and Data Systems, 5, 27–44, 2016.

Goldsmith, P. F.: Quasi-optical techniques, Proceedings of the IEEE, 80, 1729–1747, 1992.

Hallgren, K., Hartogh, P., and Jarchow, C.: A new microwave spectrometer for ground-based observations of water vapour, Atmospheric Measurement Techniques Discussions, 6, 4677–4703, 2013.

Joint, F., Lapkin, I., Vigneron, P.-B., Hérault, E., Meledin, D., Pavolotsky, A., Strandberg, M., Ferm, S. E., Fredrixon, M., Helldner, L., et al.: 3D-Structured Polyethylene Windows for Low-Loss Transmission in Wideband Cryogenic Terahertz Systems, IEEE Transactions on Terahertz Science and Technology, 2026.

Khaykin, S., Podglajen, A., Ploeger, F., Grooß, J.-U., Tencé, F., Bekki, S., Khlopenkov, K., Bedka, K., Rieger, L., Baron, A., et al.: Global perturbation of stratospheric water and aerosol burden by Hunga eruption, Communications Earth & Environment, 3, 316, 2022.

Krochin, W., Stober, G., and Murk, A.: Development of a Polarimetric 50-GHz Spectrometer for Temperature Sounding in the Middle Atmosphere, IEEE Journal of selected topics in applied earth observations and remote sensing, 15, 5644–5651, 2022.

Krochin, W., Murk, A., Luder, A., and Stober, G.: Operational calibration of a fully polarimetric radiometer for stratospheric temperature retrievals, EGUsphere, 2025, 1–28, https://doi.org/10.5194/egusphere-2025-2561, 2025.

Matoza, R. S., Fee, D., Assink, J. D., Iezzi, A. M., Green, D. N., Kim, K., Toney, L., Lecocq, T., Krishnamoorthy, S., Lalande, J.-M., Nishida, K., Gee, K. L., Haney, M. M., Ortiz, H. D., Brissaud, Q., Martire, L., Rolland, L., Vergados, P., Nippress, A., Park, J., Shani-Kadmiel, S., Witsil, A., Arrowsmith, S., Caudron, C., Watada, S., Perttu, A. B., Taisne, B., Mialle, P., Pichon, A. L., Vergoz, J., Hupe, P., Blom, P. S., Waxler, R., Angelis, S. D., Snively, J. B., Ringler, A. T., Anthony, R. E., Jolly, A. D., Kilgour, G., Averbuch, G., Ripepe, M., Ichihara, M., Arciniega-Ceballos, A., Astafyeva, E., Ceranna, L., Cevuard, S., Che, I.-Y., Negri, R. D., Ebeling, C. W., Evers, L. G., Franco-Marin, L. E., Gabrielson, T. B., Hafner, K., Harrison, R. G., Komjathy, A., Lacanna, G., Lyons, J., Macpherson, K. A., Marchetti, E., McKee, K. F., Mellors, R. J., Mendo-Pérez, G., Mikesell, T. D., Munaibari, E., Oyola-Merced, M., Park, I., Pilger, C., Ramos, C., Ruiz, M. C., Sabatini, R., Schwaiger, H. F., Tailpied, D., Talmadge, C., Vidot, J., Webster, J., and Wilson, D. C.: Atmospheric waves and global seismoacoustic observations of the January 2022 Hunga eruption, Tonga, Science, 377, 95–100, https://doi.org/10.1126/science.abo7063, 2022.

McKay, J. E., Robertson, D. A., Speirs, P. J., Hunter, R. I., Wylde, R. J., and Smith, G. M.: Compact Corrugated Feedhorns With High Gaussian Coupling Efficiency and -60 dB Sidelobes, IEEE Transactions on Antennas and Propagation, 64, 2518–2522, https://doi.org/10.1109/TAP.2016.2543799, 2016.

Millan, R., Mouginot, J., Rabatel, A., and Morlighem, M.: Ice velocity and thickness of the world's glaciers, Nature Geoscience, 15, 124–129, 2022.

Milz, M., von Clarmann, T., Fischer, H., Glatthor, N., Grabowski, U., Höpfner, M., Kellmann, S., Kiefer, M., Linden, A., Mengistu Tsidu, G., Steck, T., Stiller, G. P., Funke, B., López-Puertas, M., and Koukouli, M. E.: Water vapor distributions measured with the Michelson Interferometer for Passive Atmospheric Sounding on board Envisat (MIPAS/Envisat), Journal of Geophysical Research: Atmospheres, 110, https://doi.org/https://doi.org/10.1029/2005JD005973, 2005.

Motte, E., Ricaud, P., Gabard, B., Niclas, M., and Gangneron, F.: A 22-GHz Mobile Microwave Radiometer (MobRa) for the Study of Middle Atmospheric Water Vapor, IEEE Transactions on Geoscience and Remote Sensing, 46, 3104–3114, https://doi.org/10.1109/TGRS.2008.2000626, 2008.

Murtagh, D., Frisk, U., Merino, F., Ridal, M., Jonsson, A., Stegman, J., Witt, G., Eriksson, P., Jiménez, C., Megie, G., Noë, J. d. l., Ricaud, P., Baron, P., Pardo, J. R., Hauchcorne, A., Llewellyn, E. J., Degenstein, D. A., Gattinger, R. L., Lloyd, N. D., Evans, W. F., McDade, I. C., Haley, C. S., Sioris, C., Savigny, C. v., Solheim, B. H., McConnell, J. C., Strong, K., Richardson, E. H., Leppelmeier, G. W., Kyrölä, E., Auvinen, H., and Oikarinen, L.: An overview of the Odin atmospheric mission, Canadian Journal of Physics, 80, 309–319, https://doi.org/10.1139/p01-157, 2002.

Nedoluha, G. E., Bevilacqua, R. M., Gomez, R. M., Waltman, W. B., Hicks, B. C., Thacker, D. L., Russell III, J. M., Abrams, M., Pumphrey, H. C., and Connor, B. J.: A comparative study of mesospheric water vapor measurements from the ground-based water vapor millimeter-wave spectrometer and space-based instruments, Journal of Geophysical Research: Atmospheres, 102, 16 647–16 661, https://doi.org/https://doi.org/10.1029/97JD01095, 1997.

Nedoluha, G. E., Gomez, R. M., Hicks, B. C., Bevilacqua, R. M., Russell III, J. M., Connor, B. J., and Lambert, A.: A comparison of middle atmospheric water vapor as measured by WVMS, EOS-MLS, and HALOE, Journal of Geophysical Research: Atmospheres, 112, https://doi.org/https://doi.org/10.1029/2007JD008757, 2007.

Parrish, A., Dezafra, R., Solomon, P., and Barrett, J.: A ground-based technique for millimeter wave spectroscopic observations of stratospheric trace constituents, Radio Science, 23, 106–118, 1988.

Schranz, F., Hagen, J., Stober, G., Hocke, K., Murk, A., and Kämpfer, N.: Small-scale variability of stratospheric ozone during the sudden stratospheric warming 2018/2019 observed at Ny-Ålesund, Svalbard, Atmospheric Chemistry and Physics, 20, 10 791–10 806, https://doi.org/10.5194/acp-20-10791-2020, 2020.

Schröder, A., Murk, A., Yagoubov, P., and Patt, F.: Design and characterization of the ALMA band 5 vacuum window, IEEE Transactions on Terahertz Science and Technology, 6, 156–162, 2015.

Seele, C. and Hartogh, P.: Water vapor of the polar middle atmosphere: Annual variation and summer mesosphere Conditions as observed by ground-based microwave spectroscopy, Geophysical Research Letters, 26, 1517–1520, https://doi.org/https://doi.org/10.1029/1999GL900315, 1999.

Seele, C. and Hartogh, P.: A case study on middle atmospheric water vapor transport during the February 1998 stratospheric warming, Geophysical research letters, 27, 3309–3312, 2000.

Shi, G., Krochin, W., Sauvageat, E., and Stober, G.: Ozone and water vapor variability in the polar middle atmosphere observed with ground-based microwave radiometers, Atmospheric Chemistry and Physics, 23, 9137–9159, https://doi.org/10.5194/acp-23-9137-2023, 2023.

Shi, G., Krochin, W., Sauvageat, E., and Stober, G.: Ozone anomalies over the polar regions during stratospheric warming events, Atmospheric Chemistry and Physics, 24, 10 187–10 207, https://doi.org/10.5194/acp-24-10187-2024, 2024.

Shi, G., Liu, H., Tsutsumi, M., Gulbrandsen, N., Kozlovsky, A., Pokhotelov, D., Lester, M., Jacobi, C., Wu, K., and Stober, G.: New insights into the polar ozone and water vapor, radiative effects, and their connection to the tides in the mesosphere–lower thermosphere during major sudden stratospheric warming events, Atmospheric Chemistry and Physics, 25, 9403–9430, https://doi.org/10.5194/acp-25-9403-2025, 2025.

Speirs, P., Molina, R., Saenz, E., Yagoubov, P. M. P., and Murk, A.: Design and Measurement of Possible Wide-band 67-116 GHz ALMA Vacuum Window Anti-reflection Layers, in: 2020 14th European Conference on Antennas and Propagation (EuCAP), pp. 1–5, IEEE, 2020.

Steiner, M., Luo, B., Peter, T., Pitts, M. C., and Stenke, A.: Evaluation of polar stratospheric clouds in the global chemistry–climate model SOCOLv3.1 by comparison with CALIPSO spaceborne lidar measurements, Geoscientific Model Development, 14, 935–959, https://doi.org/10.5194/gmd-14-935-2021, 2021.

Straub, C., Murk, A., and Kämpfer, N.: MIAWARA-C, a new ground based water vapor radiometer for measurement campaigns, Atmospheric Measurement Techniques, 3, 1271–1285, 2010.

Straub, C., Tschanz, B., Hocke, K., Kämpfer, N., and Smith, A. K.: Transport of mesospheric H_2O during and after the stratospheric sudden warming of January 2010: observation and simulation, Atmospheric Chemistry and Physics, 12, 5413–5427, https://doi.org/10.5194/acp-12-5413-2012, 2012.

Thacker, D., Bevilacqua, R., Waltman, W., Pauls, T., Gomez, G., Nedoluha, G., and Schwartz, P.: Ground-based sensing of water vapor in the stratosphere and mesosphere, IEEE Transactions on Instrumentation and Measurement, 44, 355–359, https://doi.org/10.1109/19.377851, 1995.

TICRA: TICRA Tools – GRASP and CHAMP 3D, https://www.ticra.com/software/all-software/, computer software, 2024.

Ulaby, F. T., Moore, R. K., and Fung, A. K.: Microwave remote sensing: Active and passive. volume 1-microwave remote sensing fundamentals and radiometry, 1981.

Wang, L., Sun, X., Shulga, D., Forkman, P., Milinevsky, G., Han, W., Wang, X., Pylypenko, O., Shi, Y., Wang, Y., et al.: Microwave 110/115 GHz radiometer for simultaneous atmospheric ozone and carbon monoxide measurements, Measurement, 253, 117 546, 2025.

Waters, J. W., Froidevaux, L., Harwood, R. S., Jarnot, R. F., Pickett, H. M., Read, W. G., Siegel, P. H., Cofield, R. E., Filipiak, M. J., Flower, D. A., Holden, J. R., Lau, G. K., Livesey, N. J., Manney, G. L., Pumphrey, H. C., Santee, M. L., Wu, D. L., Cuddy, D. T., Lay, R. R., Loo, M. S., Perun, V. S., Schwartz, M. J., Stek, P. C., Thurstans, R. P., Boyles, M. A., Chandra, K. M., Chavez, M. C., Chen, G.-S., Chudasama, B. V., Dodge, R., Fuller, R. A., Girard, M. A., Jiang, J. H., Jiang, Y., Knosp, B. W., Labelle, R. C., Lam, J. C., Lee, K. A., Miller, D., Oswald, J. E., Patel, N. C., Pukala, D. M., Quintero, O., Scaff, D. M., Van Snyder, W., Tope, M. C., Wagner, P. A., and Walch, M. J.: The Earth Observing System Microwave Limb Sounder (EOS MLS) on the aura satellite, IEEE Transactions on Geoscience and Remote Sensing, 44, 1075 – 1092, https://doi.org/10.1109/TGRS.2006.873771, cited by: 1063, 2006.

Wright, C. J., Hindley, N. P., Alexander, M. J., Barlow, M., Hoffmann, L., Mitchell, C. N., Prata, F., Bouillon, M.and Carstens, J., Clerbaux, C., Osprey, S. M., Powell, N., Randall, C. E., and Yue, J.: Surface-to-space atmospheric waves from Hunga Tonga-Hunga Ha'apai eruption, Nature, 609, 741–746, https://doi.org/10.1038/s41586-022-05012-5, 2022.

Yagoubov, P., Mroczkowski, T., Belitsky, V., Cuadrado-Calle, D., Cuttaia, F., Fuller, G., Gallego, J.-D., Gonzalez, A., Kaneko, K., Mena, P., et al.: Wideband 67- 116 GHz receiver development for ALMA Band 2, Astronomy & Astrophysics, 634, A46, 2020.